

Asymmetric error field interaction with rotating conducting walls

C. Paz-Soldan, M. I. Brookhart, C. C. Hegna, and C. B. Forest

Citation: *Phys. Plasmas* **19**, 072511 (2012); doi: 10.1063/1.4737092

View online: <http://dx.doi.org/10.1063/1.4737092>

View Table of Contents: <http://pop.aip.org/resource/1/PHPAEN/v19/i7>

Published by the [American Institute of Physics](#).

Related Articles

Linear and nonlinear dynamics of current-driven waves in dusty plasmas
Phys. Plasmas **19**, 092115 (2012)

Plasma flows in scrape-off layer of Aditya tokamak
Phys. Plasmas **19**, 092507 (2012)

Development of a dielectric barrier discharge enhanced plasma jet in atmospheric pressure air
Phys. Plasmas **19**, 093504 (2012)

The stability of weakly ionized collisional dusty plasma in the presence of flow
Phys. Plasmas **19**, 093701 (2012)

Properties of convective cells generated in magnetized toroidal plasmas
Phys. Plasmas **19**, 082304 (2012)

Additional information on *Phys. Plasmas*

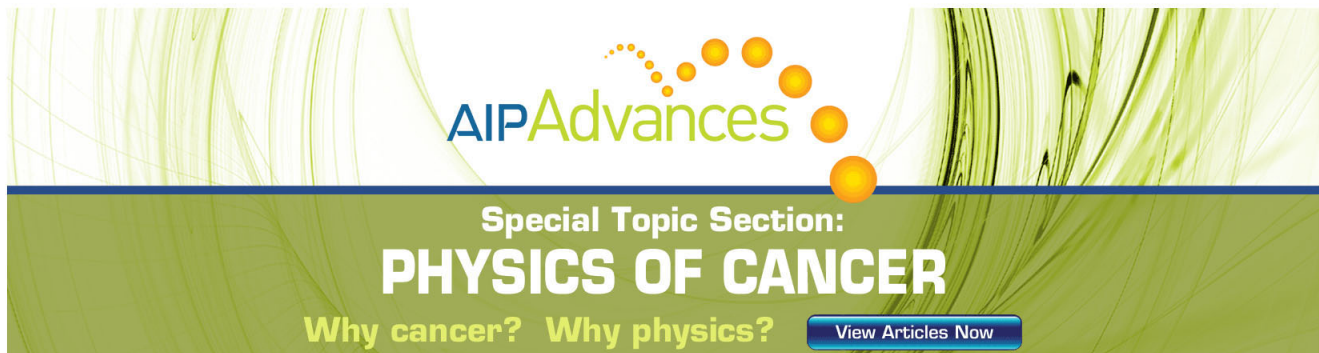
Journal Homepage: <http://pop.aip.org/>

Journal Information: http://pop.aip.org/about/about_the_journal

Top downloads: http://pop.aip.org/features/most_downloaded

Information for Authors: <http://pop.aip.org/authors>

ADVERTISEMENT



AIP Advances

Special Topic Section:
PHYSICS OF CANCER

Why cancer? Why physics? [View Articles Now](#)

Asymmetric error field interaction with rotating conducting walls

C. Paz-Soldan, M. I. Brookhart, C. C. Hegna, and C. B. Forest

Department of Physics, University of Wisconsin-Madison, Madison, Wisconsin 53706, USA

(Received 10 April 2012; accepted 12 June 2012; published online 20 July 2012)

The interaction of error fields with a system of differentially rotating conducting walls is studied analytically and compared to experimental data. Wall rotation causes eddy currents to persist indefinitely, attenuating and rotating the original error field. Superposition of error fields from external coils and plasma currents are found to break the symmetry in wall rotation direction. The vacuum and plasma eigenmodes are modified by wall rotation, with the error field penetration time decreased and the kink instability stabilized, respectively. Wall rotation is also predicted to reduce error field amplification by the marginally stable plasma. © 2012 American Institute of Physics. [<http://dx.doi.org/10.1063/1.4737092>]

I. INTRODUCTION

Plasma confinement devices inevitably contain non-axisymmetric magnetic fields due to mechanical misalignments of current-carrying elements. As these are not part of the design magnetic configuration, they are termed “error fields” (EFs). Such EFs play a critical role in these devices.^{1,2} Besides directly reducing confinement through enhanced particle drifts, EFs affect the plasma through their impact on the torque balance.³ The EF can slow the plasma rotation by applying resonant or non-resonant braking torques,^{4,5} and in certain regimes the EF can actually accelerate the plasma.⁶

As plasma flow is important to the stability of various magneto-hydrodynamic (MHD) modes, EFs are indirectly involved in determining the stability of the plasma. For example, minimizing the EF reduces braking torques which then allows the plasma flow to be sustained for longer periods which in turn increases the discharge duration.^{7–9} To complicate matters, the EF can also be amplified by the plasma itself, and this modification to the EF (called the “plasma response”) has been found to depend on the underlying stability of the plasma.^{10,11} This necessitates a sophisticated plasma model to accurately predict the total EF and thus the performance of future devices.^{12,13} EFs are also important to the accelerator community for related reasons.^{14,15}

Several studies have theoretically predicted that differential rotation of a conducting boundary can stabilize MHD modes.^{16–19} As such, they have been considered for future devices.²⁰ Topologically, rotation in toroidal geometries is only possible with flowing liquid metal. As any such future devices would unavoidably contain EFs, the interaction of the EF with rotating (or flowing) elements is of fundamental interest. Previous theoretical work including rotating elements has considered error field amplification (EFA) by the plasma,^{21–23} and the modification to the EFs in specific geometries.^{24–27}

In this study, the interaction of the EF with a rotating conducting wall is studied analytically and compared to experiments on the Rotating Wall Machine, a screw-pinch device equipped with a high-speed solid rotating wall and extensive magnetic diagnostics.²⁸ As with toroidal configura-

tions, MHD modes in this device have been found to be very sensitive to EFs, with the EF causing mode-locking and kink mode destabilization.^{29,30} Thus, understanding the interaction of the EF with wall rotation is required to understand MHD stability in this experiment. This study shows that wall rotation permanently shields the EFs from the plasma and induces a phase shift from the applied EF orientation. Superposition of EFs from distinct sources is found to lead to asymmetry in wall rotation direction, with the potential for one direction of rotation to overcome the shielding effect and increase the EF felt by the plasma. The normal modes of the rotating system are derived and it is shown that the vertical field penetration time decreases as wall rotation increases. Wall rotation is also predicted to reduce the ability of the plasma to amplify the EF.

The organization of this paper is as follows: Section II defines the geometry and derives the thin-wall matching conditions. Section III examines the $t \rightarrow \infty$ solution, as rotation induces persistent eddy currents that alter the magnetic field structure. Section IV derives the vacuum eigenmodes of the rotating wall system and studies the influence of rotation on these modes. Section V extends the formalism of this paper to study the linear stability of the plasma and treat EF amplification. Further discussion is provided in Sec. VI.

II. ANALYTICAL AND EXPERIMENTAL GEOMETRY

In this study, several wall geometries are considered. These are: a single rotating wall (Fig. 1(a)), two walls with the outer wall rotating (Fig. 1(b)), and three walls with the middle wall rotating (Fig. 1(c)). The single wall geometry is useful as it forms the building block of the multi-wall systems. The two-wall geometry contains the relevant rotating wall physics, while the three-wall geometry is required to match the experiment (whose parameters are displayed in Table I). In the device, the third wall represents the mechanical structure used to support the rotating wall. Measurements herein are made using an 8 axial by 10 azimuthal B_r fluxloop array.²⁸

Experimentally, two classes of symmetry-breaking current sources are available. The first is applied from outside the rotating wall through conductors far from the walls, as shown in Fig. 2(a). Current through this coil provides a

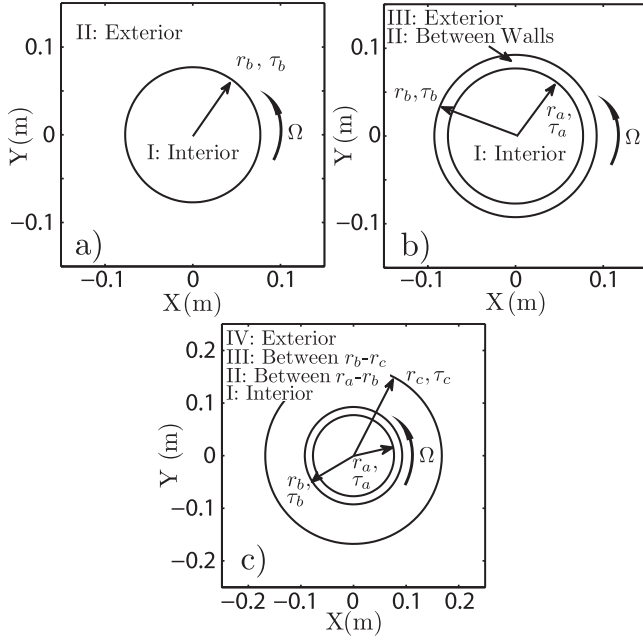


FIG. 1. Wall geometries and solution regions examined in this study with scale set to experimental parameters. (a) Single rotating wall geometry, (b) two-wall geometry, and (c) three-wall geometry.

predominantly $m = 1$ field (where m is the azimuthal wave-number) and is hereafter called \vec{B}_{ext} . Small imbalances in the resistance of conductors used to return plasma currents in the linear device can also source \vec{B}_{ext} . The second current source is that of equilibrium plasma currents whose centroid is offset from the wall geometric axis (hereafter called \vec{B}_{eq}). This offset would arise from the misalignment of the magnetic axis to the geometric axis. \vec{B}_{eq} is produced either with a current-carrying plasma or with a solid conducting rod located at radius r_r and angle η , as shown in Fig. 2(b). The field produced by this configuration is not spectrally pure, though only $m = 1$ is treated as this is the only component resonant with the kink mode in the device.

A. Vacuum region solution and boundary conditions

In the vacuum regions outside and between the rotating walls, the Laplace equation ($\nabla^2\Phi = 0$, where Φ is the magnetostatic potential) in cylindrical geometry is used to calculate the magnetostatic fields. The displacement current is neglected, and the long-cylinder approximation removes all variation in \hat{z} . As $\vec{B} = -\nabla\Phi$,

$$\begin{aligned} B_r(r, \theta) &= \Re[(A_j - A_k r^{-2})e^{-i\theta}] \\ B_\theta(r, \theta) &= \Re\left[\left(-i(A_j + A_k r^{-2})\right)e^{-i\theta}\right], \end{aligned} \quad (1)$$

TABLE I. Experimental parameters for each cylindrical wall of the rotating wall machine. For all walls, the aspect ratio (radius/length) ≈ 10 .

Wall	Radius (cm)	Wall time (ms)
Vacuum vessel	$r_a = 7.71$	$\tau_a = 3.5$
Rotating wall	$r_b = 9.16$	$\tau_b = 7.0$
Mechanical structure	$r_c = 17.30$	$\tau_c = 41.3$
Measurement array	$r_m = 8.00$	N/A

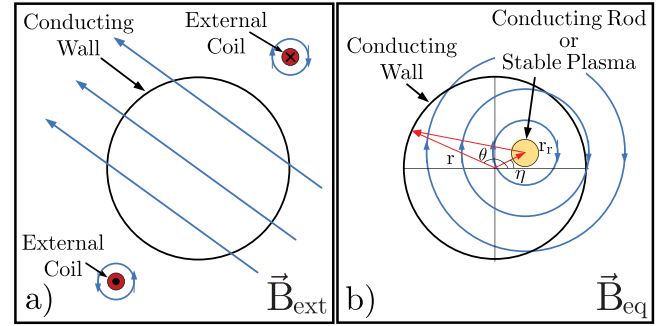


FIG. 2. Cartoons of (a) an externally applied error field (\vec{B}_{ext}) driven by a coil external to the conducting walls and (b) current applied through a conducting rod or stable plasma within the interior of the conducting walls (located at radius r_r and angle η) producing \vec{B}_{eq} .

where the guide field (B_z) is neglected. A_j, A_k are constant (complex) coefficients, and time-dependence has been left unspecified. If a current source of the form of Fig. 2(a) is present, the solution as $r \mapsto \infty$ is \vec{B}_{ext} . Thus, in this case simply $A_j = B_{\text{ext}}$, where the coordinate system is aligned with \vec{B}_{ext} . If \vec{B}_{eq} (of the form of Fig. 2(b)) is present, then the field inside the innermost conductor has a term like $B \propto r^{-2}$. The matching used is to let $A_k = b_{\text{eq}}$, where $b_{\text{eq}} = B_{\text{eq}} r^2 = -i \frac{\mu_0 I_p r_i}{2\pi} \exp(-i\eta)$ and has units of $[\text{T m}^2]$ and is thus left lowercase. I_p is the current driven (into the page) through the plasma or conducting rod at radius r_r and angle η .

B. Matching through rotating conducting walls

In the rotating/static walls, the magnetic field obeys the induction equation

$$\frac{\partial \vec{B}}{\partial t} = \underbrace{\nabla \times \vec{V} \times \vec{B}}_{\text{advection}} + \underbrace{\frac{1}{\mu_0 \sigma} \nabla^2 \vec{B}}_{\text{diffusion}}, \quad (2)$$

where σ is the (constant) conductivity of the wall. The radial projection of this vector equation is used. Enforcing $\vec{B} \propto \exp(-\gamma t)$ allows the first term in Eq. (2) to be linear in γ . For this work, γ is complex and $\equiv \gamma^r + i\omega$. Note that $\gamma^r > 0$ is a decay constant, while $\gamma^r < 0$ is a growth rate. The wall velocity is that of rigid rotation, $\vec{V} = r\Omega\hat{\theta}$. For the final term the long-cylinder identity $[\nabla^2 \vec{B}]_r = \frac{1}{r} \nabla^2(rB_r)$ is used, after which Eq. (2) becomes

$$(\gamma + i\Omega)B_r = -\frac{1}{\mu_0 \sigma r} \nabla^2(rB_r).$$

This equation is now integrated from $r_w^- \equiv r_w - \frac{\delta_w}{2}$ to $r_w^+ \equiv r_w + \frac{\delta_w}{2}$, where r_w and δ_w are the radius and thickness, respectively, of any wall. The thin-wall approximation is used which states that B_r and r_w are constant across δ_w . For this to be accurate the wall thickness δ_w must be much less than the skin depth for a given γ such that $\gamma \mu_0 \sigma \delta_w^2 \ll 1$. This is easily satisfied for the experiment as $\gamma \tau_w \ll r_w / \delta_w \approx 100$. Here, $\tau_w \equiv \mu_0 \sigma r_w \delta_w$ is called the ‘‘wall time.’’ The integration yields

$$\delta_w(\gamma + i\Omega)B_r = -\frac{1}{\mu_0\sigma r_w} \frac{\partial}{\partial r}(rB_r)|_{r=r_w^-}^{r=r_w^+}$$

$$\begin{bmatrix} 1 & r_b^{-2} \\ iR_m - 1 & r_b^{-2} \end{bmatrix} \begin{bmatrix} A_0 \\ A_1 \end{bmatrix} = \begin{bmatrix} B_{\text{ext}} \\ -B_{\text{ext}} \end{bmatrix}, \quad (6)$$

and $\nabla \cdot \vec{B} = 0$ yields $\frac{\partial}{\partial r}(rB_r) = -\frac{\partial B_\theta}{\partial \theta} = iB_\theta$. The final matching conditions are presented

$$B_r|_{r=r_w^-}^{r=r_w^+} = 0 \quad (3)$$

$$B_\theta|_{r=r_w^-}^{r=r_w^+} = i(\gamma + i\Omega)\tau_w B_r. \quad (4)$$

These conditions must be upheld at each wall, with $\Omega = 0$ if the wall is static. Note that if both $\gamma = 0$ and $\Omega = 0$ the field is not affected by the wall.

III. STEADY-STATE ERROR FIELD INTERACTIONS

Steady state field solutions ($\gamma = 0$) are strongly affected by wall rotation (Ω). The fields arising from currents external to the conducting walls (\vec{B}_{ext} , as in Fig. 2(a)) and equilibrium plasma currents internal to the conducting walls (\vec{B}_{eq} , as in Fig. 2(b)) will be first treated independently then linearly superimposed. Solutions will be calculated and compared to experimental measurements using solid conductors or a stable plasma. When $\gamma = 0$, static conducting walls do not play a role. Thus, the single wall geometry of Fig. 1(a) is used.

A. External error fields

Forcing from currents external to the rotating wall (as in Fig. 2(a)) requires that as $r \rightarrow \infty$, $\vec{B} \rightarrow \vec{B}_{\text{ext}}$. The following functional form of \vec{B} must be upheld

$$\begin{aligned} I : B_r(r, \theta) &= \Re[A_0 e^{-i\theta}] \\ II : B_r(r, \theta) &= \Re[(B_{\text{ext}} - A_1 r^{-2}) e^{-i\theta}] \end{aligned} \quad (5)$$

and where the divergence-free condition can be used to find B_θ . Using the matching conditions of Eqs. (3) and (4), the following matrix equation is generated

where $R_m \equiv \Omega\tau_w$. Equation (6) is non-homogeneous, and upon inversion yields a unique solution for A_n . The ratio of the field amplitude within the rotating wall (B_r) to the applied B_{ext} field is given by

$$\frac{|\vec{B}_r|}{B_{\text{ext}}} = \frac{1}{\sqrt{1 + \frac{R_m^2}{4}}}. \quad (7)$$

Wall rotation permanently shields the region within the rotating wall from error fields, an effect termed “flux exclusion” and clearly illustrated by the density of the fieldlines within the wall in Figs. 3(a)–3(c). Figure 3(d) compares this calculation to experimental data and the agreement is excellent. Wall rotation also introduces a phase shift (ϕ) between the applied \vec{B}_{ext} and \vec{B}_r . This is calculated using Eq. (6) to be

$$\phi = \arctan\left(\frac{R_m}{2}\right). \quad (8)$$

In the thin-wall limit, ϕ cannot exceed $\pm\pi/2$. Figure 3(e) compares this calculation to experimental data and agreement is found to be excellent. The superb agreement of Fig. 3 gives confidence that the experiment can be used to test the more complex configurations presented in the remainder of this study.

B. Equilibrium plasma currents

Forcing from plasma currents internal to the rotating wall (as in Fig. 2(b)) requires that the portion of the field decaying as r^{-2} be uniquely specified by the current source. Utilizing the single wall geometry, the following functional form of \vec{B} must be upheld

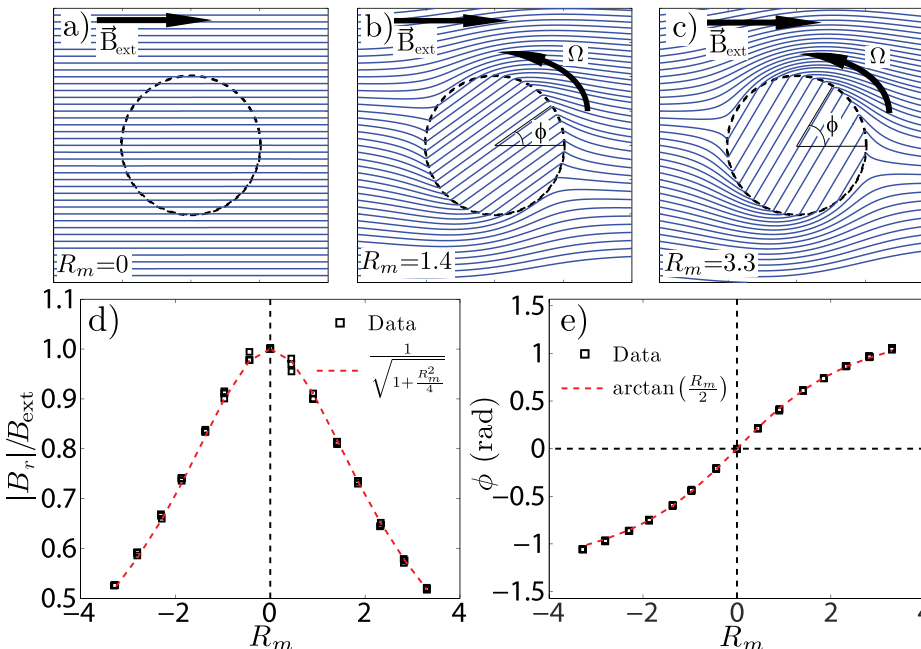


FIG. 3. (a)–(c) Fieldlines of the steady-state field created by the application of an external $m = 1$ field (\vec{B}_{ext}) with all static walls omitted for clarity. The field within the rotating wall is observed to be (d) excluded and (e) phase shifted by the persistent eddy currents in the rotating wall.

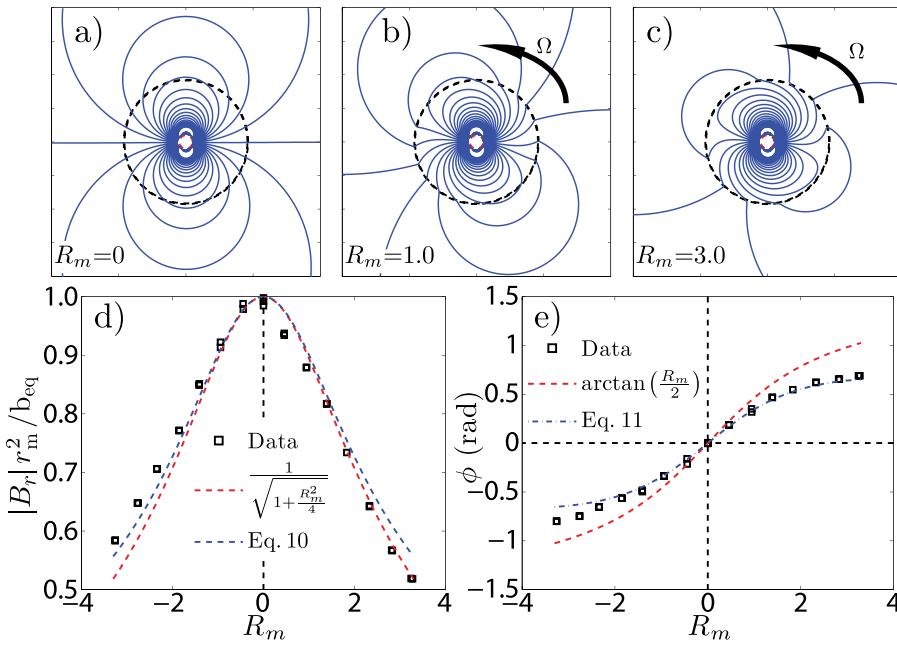


FIG. 4. (a)-(c) Fieldlines of the $m=1$ component of the steady-state field created by currents in a conducting rod or stable plasma within the rotating wall (\vec{B}_{eq}) with all static walls omitted for clarity. Field penetration through the rotating wall is found to be (d) reduced and (e) phase shifted by the persistent eddy currents in the rotating wall.

$$I : B_r(r, \theta) = \Re[(A_0 - b_{eq}r^{-2})e^{-i\theta}],$$

$$II : B_r(r, \theta) = \Re[(-A_1)r^{-2}e^{-i\theta}].$$

This is similar to Eq. (5) though with the source term b_{eq} located in the interior solution as discussed in Sec. II A. Using the matching conditions of Eqs. (3) and (4), the following matrix equation is generated

$$\begin{bmatrix} r_b^2 & 1 \\ r_b^2 & iR_m - 1 \end{bmatrix} \begin{bmatrix} A_0 \\ A_1 \end{bmatrix} = \begin{bmatrix} b_{eq} \\ -b_{eq} \end{bmatrix}. \quad (9)$$

Equation (9) is non-homogeneous, and upon inversion yields a unique solution for A_n . Solution fieldlines at various R_m are shown in Figs. 4(a)–4(c). Flux exclusion again occurs, though its form is modified from Eq. (7) and a dependence on r_m (the measurement radius) is introduced

$$\frac{|B_r|}{b_{eq}r_m^{-2}} = \frac{1}{1 + \frac{R_m^2}{4}} \sqrt{\left(1 + \alpha_m \frac{R_m^2}{4}\right)^2 + \frac{R_m^2}{4}(1 - \alpha_m)^2}, \quad (10)$$

where $\alpha_m \equiv \frac{r_b^2 - r_m^2}{r_b^2}$ has been defined and is 0.23 in the experiment. Though similar in form to Eq. (7), correction terms of $\mathcal{O}(\alpha_m)$ exist. In the limit of $r_m \mapsto r_b$ and $\alpha_m \mapsto 0$, Eq. (10) is identical to Eq. (7). Comparison to experimental data, shown in Fig. 4(d), is found to be good. The departure from the perfect agreement of Sec. III A will be discussed in Sec. III C. The observed phase shift is distinct from Eq. (8) and now also depends on r_m

$$\phi = \arctan\left(\frac{R_m}{2} \left(\frac{1 - \alpha_m}{1 + \alpha_m \frac{R_m^2}{4}}\right)\right). \quad (11)$$

Again corrections of $\mathcal{O}(\alpha_m)$ exist, and these tend to reduce the amount of phase shift observed. Similarly, in the limit of

$r_m \mapsto r_b$, Eq. (11) is identical to Eq. (8). Excellent agreement of Eq. (11) with experimental data is shown in Fig. 4(e). Unlike the case of external forcing, the effect of the rotating wall on Eqs. (10) and (11) depends on r_m and is most pronounced at $r_m = r_b$. Also, note that this field contains a finite electromagnetic torque if $R_m \neq 0$.³⁰

C. Superposition of error fields and asymmetric response

The difference between the response to \vec{B}_{ext} and \vec{B}_{eq} in flux exclusion (Eq. (7) vs Eq. (10)) and phase shift (Eq. (8) vs Eq. (11)) gives rise to an asymmetry in wall rotation direction. To illustrate this simply, the linear superposition of \vec{B}_{ext} and \vec{B}_{eq} is checked for parity. $\vec{B}_{ext} = B_{ext} \exp(i(\phi_e(R_m) - \phi_{0e}))$ and $\vec{B}_{eq} = B_{eq} \exp(i(\phi_i(R_m) - \phi_{0i}))$, where $\phi_e(R_m)$ is Eq. (8) and $\phi_i(R_m)$ is Eq. (11). All amplitude informations (Eqs. (7) and (10)) is ignored for simplicity and both source terms are separated at $R_m = 0$ by an angle $\Delta\phi_0 \equiv \phi_{0e} - \phi_{0i}$. Parity at $+R_m$ and $-R_m$ is checked

$$\begin{aligned} &= |\vec{B}_{ext} + \vec{B}_{eq}|_{+R_m}^2 - |\vec{B}_{ext} + \vec{B}_{eq}|_{-R_m}^2 \\ &= 2B_{ext}B_{eq}(\cos(\Delta\phi - \Delta\phi_0) - \cos(-\Delta\phi - \Delta\phi_0)) \\ &= 4B_{ext}B_{eq}\sin(\Delta\phi)\sin(\Delta\phi_0), \end{aligned} \quad (12)$$

where $\Delta\phi \equiv \phi_e(R_m) - \phi_i(R_m)$ is the difference between Eqs. (8) and (11). Since $\Delta\phi \neq 0$, Eq. (12) is non-zero. Asymmetry in R_m is maximized when $\Delta\phi_0 = \pm \frac{\pi}{2}$.

This asymmetry is demonstrated experimentally by pulsing \vec{B}_{ext} and \vec{B}_{eq} simultaneously. Inclusion of both \vec{B}_{ext} and \vec{B}_{eq} using the full vector superpositions of Eqs. (7), (8) and (10), (11) is shown in Figs. 5(a) and 5(b) for two different $\Delta\phi_0$, each separated by π . Changing $\Delta\phi_0$ by π is done by repositioning the conducting rod (changing the angle η in Fig. 2(b)). The resultant asymmetry in flux exclusion is captured by the model, as is the asymmetry reversal as $\Delta\phi_0 \mapsto \Delta\phi_0 + \pi$. Note that Fig. 5(b) shows the same data of

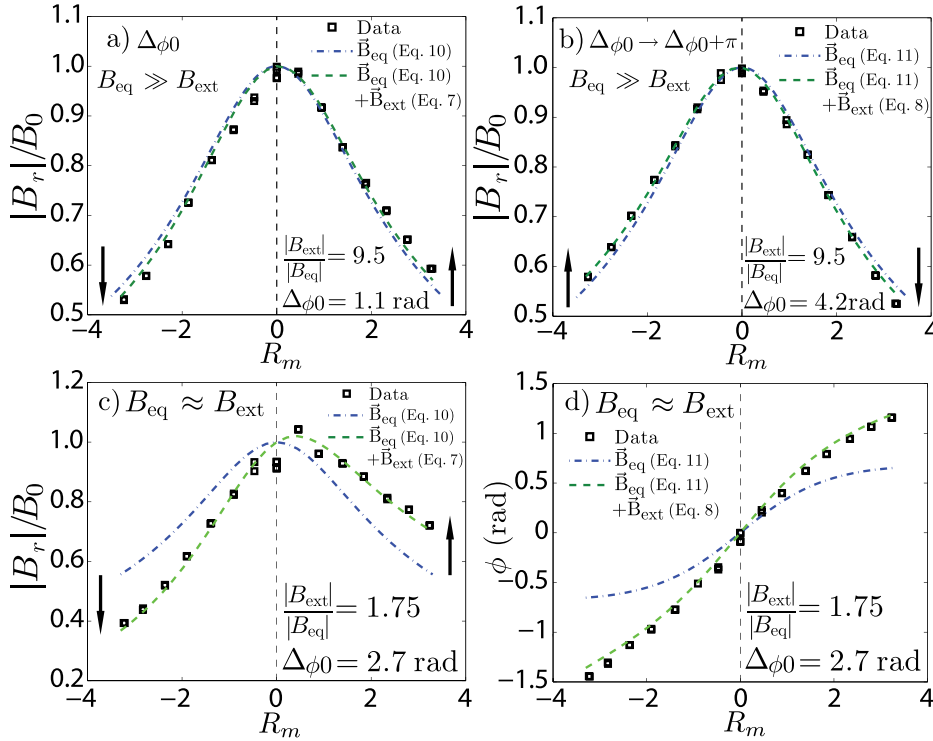


FIG. 5. Asymmetry in R_m in (a) flux exclusion in the presence of both \vec{B}_{eq} (conducting rod) and \vec{B}_{ext} . For a given $\Delta\phi_0$, flux exclusion is reduced at $R_m > 0$ while (b) changing $\Delta\phi_0 \mapsto \Delta\phi_0 + \pi$ reverses the asymmetry. (c) and (d) With suitably chosen \vec{B}_{ext} , \vec{B}_{eq} , and $\Delta\phi_0$, the asymmetry can become very large and overwhelm the shielding effect of wall rotation.

Fig. 4(d), where much better agreement is found when \vec{B}_{ext} is included. Although in Figs. 5(a) and 5(b) this asymmetry is a small correction, it can be made large if $B_{eq} \approx B_{ext}$, as shown in Figs. 5(c) and 5(d). If $B_{eq} \approx B_{ext}$ and $\Delta\phi_0 \approx \pi$, as would be the case if external currents were used to correct the misalignment of the magnetic axis,³¹ increasing R_m would increase the error field significantly.

D. Asymmetric response in plasma discharges

Strong asymmetry in R_m is also observed when the conducting rod is replaced with a stable plasma. Low current, stable plasmas are used to isolate the interaction of equilibrium currents (\vec{B}_{eq}) with \vec{B}_{ext} without considering MHD instabilities. Figure 6 illustrates large asymmetry in plasma discharges. The scatter in the data is also larger due to the poorer reproducibility of the plasma discharge. Figures 6(a) and 6(b) illustrate a response approaching linearity in R_m , and the interactions of the error fields with the rotating wall are clearly a zeroth order effect. The error field asymmetry is found to be invariant with guide field (B_z) reversal, thus ruling out plasma drift effects. Figures 6(c) and 6(d) illustrate another plasma case where the constructive and destructive interference between \vec{B}_{ext} and \vec{B}_{eq} is dramatically demonstrated. A minimum in the total amplitude occurs at $R_m \approx 2$, which the model can capture with suitable selection of free parameters B_{ext}/B_{eq} and $\Delta\phi_0$. A wide family of curves can be generated depending on the values of B_{ext}/B_{eq} and $\Delta\phi_0$.

Figure 7 illustrates the odd parity of the asymmetric interaction with R_m and \vec{B}_{ext} . While the asymmetry in R_m is present at all B_{ext} , its sense (or parity) is inverted as \vec{B}_{ext} is reversed. That the asymmetry was not reversed upon inversion of B_z , yet was inverted with \vec{B}_{ext} gives confidence that even in the presence of a (stable) plasma, the

error field interaction can be well described by the linear superposition of B_{ext} and B_{eq} . That is, the stable plasma (Fig. 6) can be described by the same model as the conducting rod (Fig. 5). The unstable plasma will be treated in Sec. V and the effectiveness of this model will be further discussed in Sec. VI.

IV. VACUUM FIELD EIGENMODES AND VERTICAL FIELD PENETRATION

Normal mode analysis is used to derive the time-dependent behavior of the device error fields and corroborates the experimental observation that the vertical field penetration time (τ_{vfp}) decreases as R_m increases. As all equations used in Sec. II are linear in \vec{B} , the system can be expressed as an eigenvalue equation with corresponding eigenvalues and eigenvectors (normal modes) in the absence of any forcing (current sources). The normal modes of multiple wall systems will be considered, beginning with the limiting cases of a single wall and static double walls, then proceeding to the differentially rotating system and concluding with the three-wall system necessary to match experimental data.

To solve the normal modes of the system, a matching problem is carried out in a similar style to that of Sec. III, where now exponential time dependence is introduced ($Q(t) \propto Qe^{-\gamma t}$, for any Q). The two-wall geometry of Fig. 1(b) is used. The field solutions are

$$I : B_r(r, \theta, t) = \Re[A_0 e^{-i\theta}],$$

$$II : B_r(r, \theta, t) = \Re[(A_1 - A_2 r^{-2}) e^{-i\theta}],$$

$$III : B_r(r, \theta, t) = \Re[(-A_3 r^{-2}) e^{-i\theta}].$$

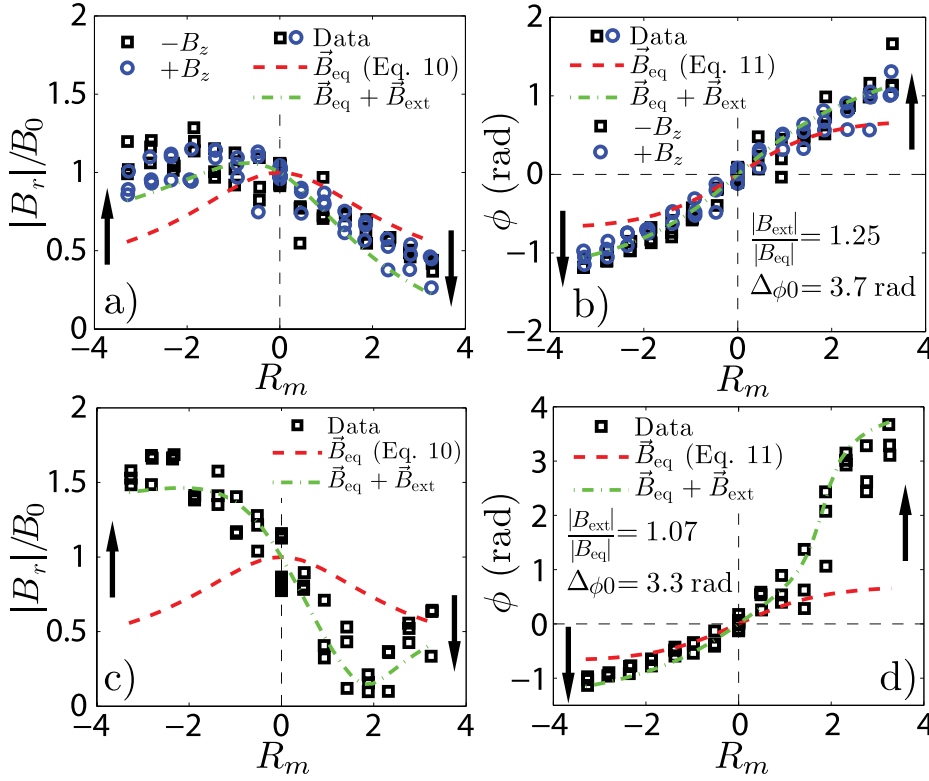


FIG. 6. Error field asymmetries in R_m in stable plasma discharges. Amplitude (a) and phase (b) of the total error field are found to be asymmetric in R_m , and the asymmetry is invariant to B_z reversal. Amplitude (c) and phase (d) indicate that extreme asymmetries are possible depending on the alignment of \vec{B}_{ext} to \vec{B}_{eq} .

The matching conditions of Eqs. (3) and (4) yield a 4×4 matrix equation for the 4 unknown parameters

$$\begin{bmatrix} -1 & 1 & -r_a^{-2} & 0 \\ \gamma\tau_a - 1 & 1 & r_a^{-2} & 0 \\ 0 & 1 & -r_b^{-2} & r_b^{-2} \\ 0 & r_b^2 & 1 & (\gamma + i\Omega)\tau_b - 1 \end{bmatrix} \begin{bmatrix} A_0 \\ A_1 \\ A_2 \\ A_3 \end{bmatrix} = 0. \quad (13)$$

Setting the determinant of the matrix of Eq. (13) to zero yields the characteristic equation

$$(\tau_a\tau_b\alpha)\gamma^2 - (2(\tau_a + \tau_b) - i\Omega\tau_a\tau_b\alpha)\gamma + 2(-2 + i\Omega\tau_b) = 0, \quad (14)$$

where defining $\alpha \equiv \frac{r_b^2 - r_a^2}{r_a^2 r_b^2}$ replaces the geometry of the problem with a normalized mutual inductance. Two normal modes exist, and the equation for the roots of Eq. (14) is then decomposed into real and imaginary terms

$$\gamma^r = \frac{\tau_a + \tau_b}{\tau_a\tau_b\alpha} \pm \frac{(\kappa_r^2 + \kappa_i^2)^{\frac{1}{4}}}{\tau_a\tau_b\alpha} \cos\left(\frac{1}{2} \arctan\left(\frac{\kappa_i}{\kappa_r}\right)\right) \quad (15)$$

$$\omega = -\frac{\Omega}{2} \pm \frac{(\kappa_r^2 + \kappa_i^2)^{\frac{1}{4}}}{\tau_a\tau_b\alpha} \sin\left(\frac{1}{2} \arctan\left(\frac{\kappa_i}{\kappa_r}\right)\right) \quad (16)$$

$$\kappa_r \equiv (\tau_a + \tau_b)^2 - 4\tau_a\tau_b\alpha - \frac{\Omega^2}{4} (\tau_a\tau_b\alpha)^2$$

$$\kappa_i \equiv \Omega\tau_a\tau_b\alpha(\tau_b - \tau_a).$$

To explore the behavior of Eqs. (15) and (16), limiting cases with respect to rotation (Ω) and mutual inductance (α) are treated separately.

A. Single wall limit

The simplest case to consider is that of Fig. 1(a), with only a single wall which is allowed to rotate. This is achieved by letting $\tau_a \mapsto 0$ in Eqs. (15) and (16). In this limit, only a single root remains, which is given by

$$\gamma = \frac{2}{\tau_b} - i\Omega. \quad (17)$$

The real part of this eigenvalue ($\Re[\gamma] \equiv \gamma^r \equiv \frac{1}{\tau_{\text{vip}}} = \frac{2}{\tau_a}$) is the unique time constant characterizing eddy current decay (and thus vertical field penetration) in the single wall system. Furthermore, γ^r does not depend on Ω ; wall rotation in the single wall case merely transforms the normal mode into a rotating frame with $\omega = \Omega$. The eigenfunction (field structure) is given by: $A_0 = A_1 = -r_b^{-2}A_3$, $A_2 = 0$, which yields a dipole-like solution as shown in Fig. 8. As this is an infinite-length model, the wall eddy currents flow purely into and out of the

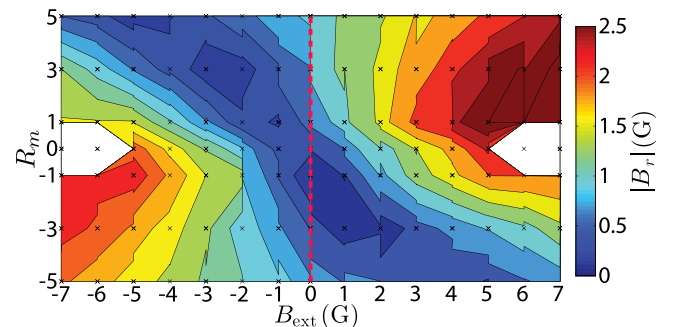


FIG. 7. Contour plot of measured radial magnetic field (B_r) as B_{ext} and R_m are varied. The error field asymmetry in R_m is inverted upon B_{ext} reversal. Operation limits prevented data collection at large B_{ext} and low R_m .

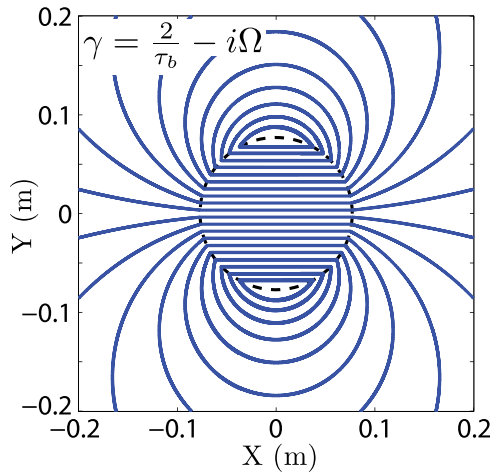


FIG. 8. Fieldlines of \vec{B} produced by the eddy current eigenfunction in a single wall. Current flows into and out of the page as $J_z \propto \delta(r - r_w) \exp(-i\theta)$, producing a constant field within the wall and dipolar field beyond. This structure is independent of rotation for the single wall case.

page, while in a finite-length wall these currents must close at the ends giving rise to fringing fields.

B. Static double wall limit

In the limit of no rotation ($\Omega \mapsto 0$), Eqs. (15) and (16) become

$$\gamma = \frac{1}{\tau_a \tau_b \alpha} \left[\tau_a + \tau_b \pm [(\tau_a + \tau_b)^2 - 4\alpha \tau_a \tau_b]^{\frac{1}{2}} \right]. \quad (18)$$

To begin, the large gap limit of $\alpha \mapsto 1$, $r_b \gg r_a$ is also taken. In this limit, $\gamma = \left\{ \frac{2}{\tau_a}, \frac{2}{\tau_b} \right\}$ and each normal mode is independently tied to its own wall and has the single wall time constant of Eq. (17). Thus, α behaves as a mutual inductance between the two walls. Figure 9 shows the behavior of γ as $\alpha \neq 1$. Both γ diverge from their decoupled values and a fast and slow root develops. For experimental parameters, $\gamma_1 \approx 10\gamma_2$. The asymptote of strong coupling (small gap, $\alpha \mapsto 0$) corresponds to the same solution as a single wall system with $\tau = \tau_a + \tau_b$ and the fast root decaying infinitely quickly.

For weak coupling ($\alpha \mapsto 1$), the eigenfunctions are the same as Fig. 8. Eigenfunctions with the coupling parameter set to that of the experiment ($\alpha_{\text{exp}} = 0.3$) are next considered. As shown in Figs. 9(b) and 9(c), the γ_1 (fast) eigenfunction is confined to within the two-wall system, while the γ_2 (slow) eigenfunction is dipolar everywhere. In terms of induced eddy currents, the γ_1 currents are counter-aligned in each wall, while the γ_2 currents are co-aligned, thus they can be thought of as opposing and reinforcing dipoles, respectively. Qualitatively, this is reminiscent of the coupled oscillator, whose eigenmodes are symmetric and anti-symmetric oscillations.

C. Effect of wall rotation

Wall rotation is now reintroduced, necessitating the full form of Eqs. (15) and (16) and yielding complex eigenvalues

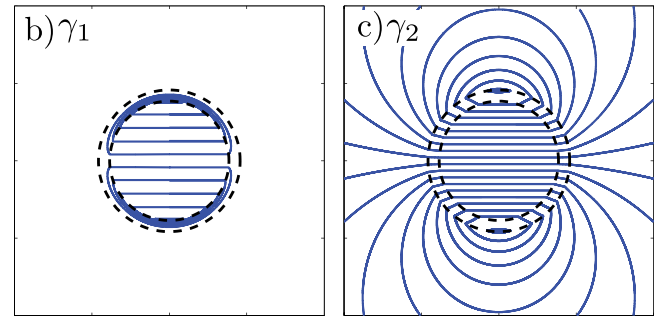
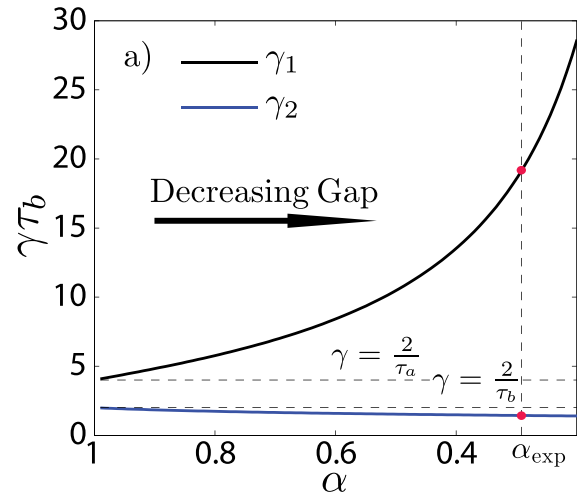


FIG. 9. (a) Time constants (eigenvalues) of the static two-wall normal modes as the coupling parameter α varies. (b) and (c) Eigenstructure of the normal modes of (a). The fast (slow) root field structure does not (does) extend beyond the outer wall and thus represents counter- (co-) directed currents within each wall, respectively.

($\gamma \equiv \gamma^r + i\omega$). The value of Ω now affects both γ^r as well as ω , as shown in solutions for experimental parameters plotted in Fig. 10(a). Increasing R_m brings the two eigenvalues toward each other. Eigenfunctions are shown in Figs. 10(b) and 10(c) for the intermediate rotation case. Rotation is seen to phase shift the eigenfunctions in opposite directions. As with the static solution, one eigenfunction penetrates the outer wall while the other does not.

With $\Omega \mapsto \infty$ in Eqs. (15) and (16), $\gamma = \left\{ \frac{2}{\tau_a \alpha}, \frac{2}{\tau_b \alpha} - i\Omega \right\}$. The corresponding eigenfunctions are shown in Figs. 10(d) and 10(e). The γ_1 eigenfunction is found to decay at a geometrically weighted τ_a timescale, and does not extend into the rotating wall. Similarly, the γ_2 eigenfunction does not see the static wall, and as such it rotates at $\omega = \Omega$ and decays at a geometrically weighted τ_b timescale. The phase shifts have also reached an asymptotic limit of $\phi = \frac{\pi}{2}$. The fast rotation limit is thus seen to decouple the two walls, acting opposite to the coupling parameter α . The α parameter splits the eigenvalues into a slow and fast branch, while rotation brings both branches back to their (geometrically weighted) single wall values.

D. Three-wall eigenmodes and comparison to experiment

As discussed in Sec. II, a three-wall system is required to adequately capture experimental vertical field penetration data. The geometry (to scale) is presented in Fig. 1(c), with

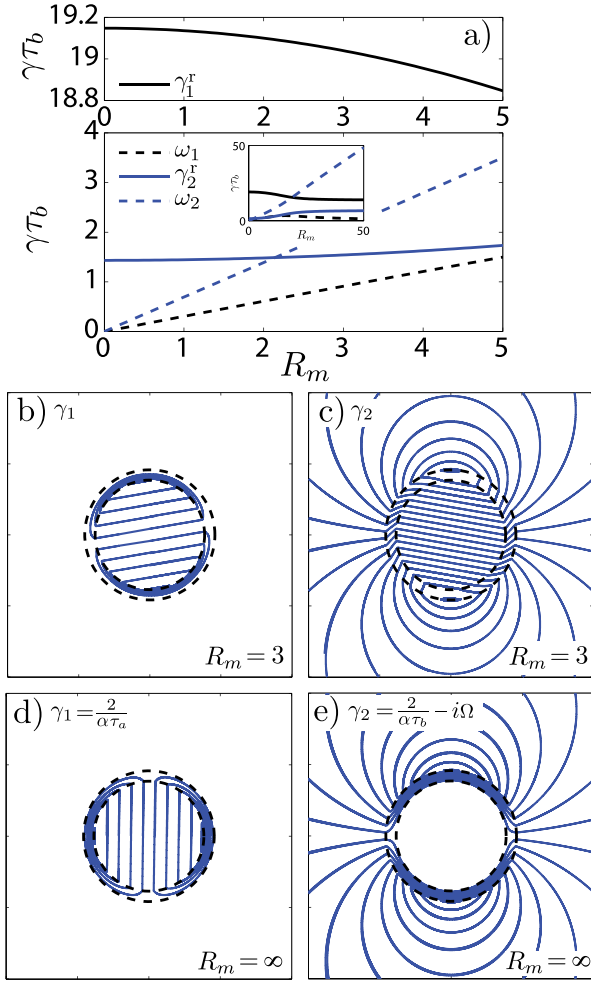


FIG. 10. (a) Real (γ^r) and imaginary (ω) time constants of the two-wall normal modes with $\Omega \neq 0$ ($R_m \equiv \Omega\tau_b$). Eigenfunctions of (b) the fast root and (c) the slow root at intermediate R_m . Eigenfunctions of (d) the fast root and (e) the slow root as $\Omega \mapsto \infty$.

the third (outermost) wall corresponding to the mechanical support structure. Fields for this geometry must be of the form

$$\begin{aligned}
 I : B_r(r, \theta, t) &= \Re[A_0 e^{-i\theta}], \\
 II : B_r(r, \theta, t) &= \Re[(A_1 - A_2 r^{-2}) e^{-i\theta}], \\
 III : B_r(r, \theta, t) &= \Re[(A_3 - A_4 r^{-2}) e^{-i\theta}], \\
 IV : B_r(r, \theta, t) &= \Re[(-A_5 r^{-2}) e^{-i\theta}],
 \end{aligned}$$

the matching conditions of Eqs. (3) and (4) are applied, which then forms a 6×6 matrix equation for the unknown A_n . For brevity, only the characteristic equation yielded by setting the determinant to zero is shown

$$\begin{aligned}
 0 &= a\gamma^3 + b\gamma^2 + c\gamma + d \quad (19) \\
 a &= \tau_a \tau_b \tau_c \alpha_1 \alpha_2 \\
 b &= 2(\tau_a \tau_b \alpha_1 + \tau_b \tau_c \alpha_2 + \tau_a \tau_c \alpha_{12}) + i\Omega \tau_a \tau_b \tau_c \alpha_1 \alpha_2 \\
 c &= 4(\tau_a + \tau_b + \tau_c) + i2\Omega(\tau_a \tau_b \alpha_1 + \tau_b \tau_c \alpha_2) \\
 d &= 4(-2 + i\Omega \tau_b).
 \end{aligned}$$

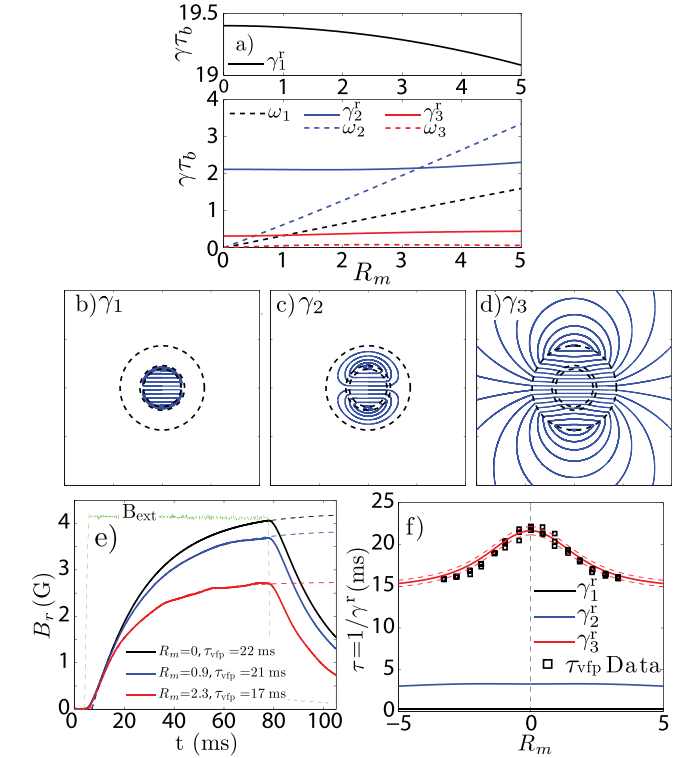


FIG. 11. (a) Eigenvalues of the three-wall normal modes. (b)–(d) Eigenfunctions of each root with $\Omega = 0$. (e) Experimental excitation of the normal modes pulsing B_{ext} and resultant measurement of the vertical field penetration time (τ_{vfp}). (f) Comparison of τ_{vfp} with γ_3^r evaluated using the experimental parameters of Table I. Dotted lines in (f) are evaluated with $\tau_c \pm 2\%$.

Again, coupling parameters are defined which simplify the geometry: $\alpha_1 \equiv \frac{r_a^2 - r_b^2}{r_b^2}$, $\alpha_2 \equiv \frac{r_b^2 - r_c^2}{r_c^2}$, $\alpha_{12} \equiv \frac{r_a^2 - r_c^2}{r_c^2}$. Beyond these simplifications, analytic forms for the three roots of Eq. (19) are prohibitively lengthy and are not shown. Solutions of Eq. (19) are shown in Fig. 11(a) and indicate that rotation affects the three-wall eigenvalues in broadly the same manner as the two-wall eigenvalues of Sec. IV C. For experimental parameters, there is one fast root which decreases as R_m increases, and two slow roots which increase as R_m increases. Eigenfunctions at $R_m = 0$ are shown in Figs. 11(b)–11(d) and illustrate that the fastest root γ_1 does not penetrate the second (rotating) wall, the middle root γ_2 does not penetrate the third wall, while the slowest root γ_3 penetrates all walls.

The inclusion of the third wall permits quantitative comparison to experiment. The normal modes are experimentally excited by the application of a square-wave B_{ext} pulse, yielding the time-traces of Fig. 11(e). The steady-state response created by this excitation has already been discussed in Sec. III A. Focusing on the time-dependent behavior shows that the vertical field penetration time (τ_{vfp}) decreases as R_m increases. As γ_3 is the most persistent eddy current, it dominates the measurement a short time after the current pulse turn-on. Figure 11(f) confirms the counter-intuitive result that increasing wall rotation (Ω) decreases τ_{vfp} . The slowest root of Eq. (19) matches the τ_{vfp} data very closely despite the fact that there are no free parameters. The dotted lines in Fig. 11(f) plot the γ_3^r root with τ_c varied by ± 1 ms (or 2%), which is sufficient to bound the data.

V. PLASMA INSTABILITIES AND ERROR FIELD AMPLIFICATION

While the results of the preceding sections apply to either vacuum or stable-plasma configurations, the inclusion of a model for the linear plasma instabilities allows for an examination of the interaction of the kink mode with wall rotation and device error fields. A plasma model will first be presented and then applied to find the normal modes (instabilities) in both the single wall and double wall limits. Error field amplification by the plasma will then be considered.

A. Description of plasma model

The plasma of the rotating wall machine is modeled using an ideal MHD treatment described in Ref. 19 which is here briefly summarized. A screw-pinch equilibrium is first defined, in which the equilibrium field, $B_0 = B_{z0}(r)\hat{z} + B_{\theta0}(r)\hat{\theta}$ is axisymmetric and invariant in \hat{z} . The plasma is taken to be force free (such that $\nabla p_0 = 0$, and $\nabla \times B_0 = \frac{\lambda(r)}{\mu_0}B_0$) and have radius r_p . The equilibrium current profile is taken to be constant within this radius and zero outside such that $\lambda = \lambda_0\Theta(r - r_p)$, where $J_0(r) \equiv \frac{\lambda(r)}{\mu_0}B_0(r)$. For this simple equilibrium, the safety factor $q(r)$ is constant for $r < r_p$ and is given by $q(r_p) = \frac{4\pi^2 r_p^2 B_z}{\mu_0 L r_p}$, where L is the device length. For $r > r_p$, $q(r)$ increases quadratically. An eigenvalue approach is taken to solve for the unstable modes. Taking $Q(t) \propto Qe^{-\gamma t}$ (for any Q , where $\gamma \equiv \gamma^r + i\omega$), the momentum and induction equations are linearized, yielding

$$\gamma^2 \rho_0 \tilde{\xi} = \tilde{J} \times B_0 + \frac{\lambda}{\mu_0} B_0 \times \tilde{B} - \nabla \tilde{p}, \quad (20)$$

$$\tilde{B} = \nabla \times (\tilde{\xi} \times B_0), \quad (21)$$

where ρ_0 is the (constant) mass density, and the displacement vector $\tilde{\xi}$ is introduced. The differential equations of Eqs. (20) and (21) are made algebraic by simplification of spatial gradients. However, due to the line-tied property of the device Fourier decomposition is only allowed in θ . Hence, $\tilde{\xi}$ and \tilde{B} can be written $\tilde{\xi} = \tilde{\xi}(r, z)e^{-i\theta}$ and $\tilde{B} = \tilde{B}(r, z)e^{-i\theta}$ (only $m = 1$ kink modes are treated). In this simplified equilibrium radial gradients in Eqs. (20) and (21) only exist at r_p . Thus, the radial derivative is substituted with algebraic ‘‘jump parameters,’’ given for \tilde{B}_r as

$$\Delta_+ = \frac{1}{\tilde{B}_r} \frac{d}{dr} (r \tilde{B}_r)_{r=r_p^+} \quad (22)$$

with similar definitions for jumps in $\tilde{\xi}$. Solutions of the resultant partial differential equation yield two allowable Fourier modes in z ($f(z) \propto e^{ikz}$). Equations (20) and (21) thus result in a quadratic equation for k , whose solutions are

$$k_{1,2} = -\frac{B_{\theta r_p}}{r_p B_{z0}} + \frac{\lambda_0}{2(1 - \Delta_+)} \pm \sqrt{\frac{\lambda_0^2}{4(1 - \Delta_+)^2} + \frac{\gamma^2}{v_A^2(1 - \Delta_+)}} \quad (23)$$

where $v_A \equiv B_{z0}^2/\mu_0\rho_0$. The boundary condition of line-tying relates the two k to one another, forming the dispersion relationship. Line-tying requires that $\tilde{\xi}_r(z=0) = \tilde{\xi}_r(z=L) = 0$. Thus, $\tilde{\xi}$ must be a linear combination of both k whose relationship is quantized such that $k_1 - k_2 = \frac{2n\pi}{L}$. Equation (23) thus becomes

$$n = \sqrt{\frac{4}{(q(r_p))^2(1 - \Delta_+)^2} + \frac{4\gamma^2\tau_A^2}{1 - \Delta_+}}, \quad (24)$$

where $\tau_A \equiv L/2\pi v_A$. The instabilities of interest have $\gamma\tau_w \approx 1$ and $\tau_w \gg \tau_A$. Thus, $\gamma\tau_A \ll 1$ and the second term in the square root of Eq. (24) is negligible. The dispersion relation (for $n = 1$) is simply

$$1 - \Delta_+ = \frac{2}{q(r_p)}. \quad (25)$$

The problem has thus been reduced to a determination of the jump parameter Δ_+ , which is computed by solving another matching problem. With vacuum assumed to fill the annulus $r_p < r < r_a$, the functional form of the field in the two-wall geometry shown in Fig. 1(b) is

$$I : B_r(r, \theta, t) = \Re[(A_0 - A_1 r^{-2})e^{-i\theta}],$$

$$II : B_r(r, \theta, t) = \Re[(A_2 - A_3 r^{-2})e^{-i\theta}],$$

$$III : B_r(r, \theta, t) = \Re[(B_{\text{ext}} - A_4 r^{-2})e^{-i\theta}],$$

where external forcing of the form of Fig. 2(a) has been included. In addition to the standard matching conditions at the conducting walls (Eqs. (3) and (4)), the jump condition of Eq. (22) yields another matching condition

$$\Delta_+ = \frac{A_0 + A_1 r_p^{-2}}{A_0 - A_1 r_p^{-2}} \quad (26)$$

$$r_p^2 \delta A_0 = A_1,$$

where shorthand notation $\delta \equiv -\left(\frac{1 - \Delta_+}{1 + \Delta_+}\right) = \frac{1}{1 - q(r_p)}$ is introduced. Using Eq. (26) in conjunction with Eqs. (3) and (4) allows a 5×5 matrix to be formed for the unknown A_n coefficients. However, in contrast to Sec. IV, the time dependence will here be left general. Furthermore, as the matrix is sparse, it can be reduced to an equivalent coupled differential equation, given by

$$\underbrace{\begin{bmatrix} \overbrace{\left[\begin{array}{cc} \left(\frac{2r_a^2 r_p^2 \delta}{r_a^2 - r_p^2 \delta} \right) & \left(\frac{-2r_a^2}{r_a^2 - r_p^2 \delta} \right) \\ r_b^2(2 - iR_m) & iR_m \end{array} \right]}^{\tilde{M}} & \overbrace{\begin{bmatrix} A_2 \\ A_3 \end{bmatrix}}^{\tilde{A}} \\ \underbrace{\begin{bmatrix} -r_a^2 \tau_a & \tau_a \\ -r_b^2 \tau_b & \tau_b \end{bmatrix}}_{\tilde{D}} & \underbrace{\frac{\partial}{\partial t} \begin{bmatrix} A_2 \\ A_3 \end{bmatrix}}_{\tilde{B}_{\text{ext}}} \end{bmatrix} = \begin{bmatrix} 0 \\ 2B_{\text{ext}} r_b^2 \end{bmatrix}, \quad (27)$$

where $A_0 = \frac{A_2 r_a^2 - A_3}{r_a^2 - r_p^2 \delta}$, $A_1 = r_p^2 \delta \left(\frac{A_2 r_a^2 - A_3}{r_a^2 - r_p^2 \delta} \right)$, $A_4 = B_{\text{ext}} r_b^2 - A_2 r_b^2 + A_3$ can be used to find the remaining coefficients.

This equation can now be solved both for the normal modes (by setting $\vec{B}_{\text{ext}} = 0$) and for steady-state error field amplification (by setting $\frac{\partial}{\partial t} \mapsto 0$).

B. Plasma normal modes (kink instabilities)

Equation (27) shows that for a given Δ_+ a unique set of eigenmodes is present in the system, allowing a prediction for the instability decay/growth rate ($\Re[\gamma] \equiv \gamma^r$) and rotation frequency ($\Im[\gamma] \equiv \omega$). To find the eigenmodes of the system, the forcing (\vec{B}_{ext}) is set to zero and the characteristic equation for γ is formed by solving $\det(\bar{M} + \gamma\bar{D}) = 0$ in Eq. (27), yielding

$$0 = a\gamma^2 + b\gamma + c \tag{28}$$

$$\begin{aligned} a &= \tau_a \tau_b (1 - \alpha_b)(1 - \alpha_p \delta) \\ b &= -2[\tau_a \alpha_b (1 - \alpha_p \delta) + \tau_b (\alpha_b - \alpha_p \delta)] \\ &\quad - i\tau_a R_m (1 - \alpha_b)(1 - \alpha_p \delta) \\ c &= -4\alpha_b + i2R_m (\alpha_b - \alpha_p \delta) \end{aligned}$$

whose solution can be given by decomposing into real and imaginary terms

$$\begin{aligned} \gamma^r &= \frac{1}{\tau_b} \left(\frac{\alpha_b}{1 - \alpha_b} \right) + \frac{1}{\tau_a} \left(\frac{(\alpha_b - \alpha_p \delta)}{(1 - \alpha_b)(1 - \alpha_p \delta)} \right) \\ &\quad \pm (\eta_r^2 + \eta_i^2)^{\frac{1}{2}} \cos \left(\frac{1}{2} \arctan \left(\frac{\eta_i}{\eta_r} \right) \right), \end{aligned} \tag{29}$$

$$\omega = \frac{\Omega}{2} \pm (\eta_r^2 + \eta_i^2)^{\frac{1}{2}} \sin \left(\frac{1}{2} \arctan \left(\frac{\eta_i}{\eta_r} \right) \right), \tag{30}$$

$$\begin{aligned} \eta_r &\equiv \frac{1}{\tau_b^2} \left(\frac{\alpha_b}{1 - \alpha_b} \right)^2 + \frac{1}{\tau_a^2} \left(\frac{(\alpha_b - \alpha_p \delta)}{(1 - \alpha_b)(1 - \alpha_p \delta)} \right)^2 \\ &\quad + \frac{2\alpha_b}{\tau_a \tau_b} \left(\frac{2 - \alpha_b - \alpha_p \delta}{(1 - \alpha_p \delta)(1 - \alpha_b)^2} \right) - \frac{\Omega^2}{4} \\ \eta_i &\equiv - \left(\frac{\Omega}{1 - \alpha_b} \right) \left[\frac{1}{\tau_a} \frac{\alpha_b - \alpha_p \delta}{(1 - \alpha_p \delta)} - \frac{\alpha_b}{\tau_b} \right], \end{aligned}$$

where non-dimensional coupling terms $\alpha_b \equiv \frac{r_b^2}{r_a^2}$ and $\alpha_p \equiv \frac{r_p^2}{r_a^2}$ have been used. As Eqs. (29) and (30) are lengthy, limiting cases are considered.

1. Single wall limit

The single wall limit (shown in Fig. 1(a)) is found by letting $\tau_a \mapsto 0$ in Eqs. (29) and (30). There is now only one solution for γ , given by

$$\gamma = \left(\frac{2}{\tau_b} \right) \frac{1 - q(r_p)}{1 - \alpha_p - q(r_p)} - i\Omega, \tag{31}$$

where $\delta \equiv (1 - q(r_p))^{-1}$ has been used. The behavior of $\Re[\gamma] \equiv \gamma^r$ as a function of $q(r_p)$ is plotted in Fig. 12(a). The instability threshold is at $q(r_p) = 1$, matching the Kruskal-Shafranov^{32,33} condition. The ideal-wall stability limit is also found (at $q(r_p) = 0.5$ for sample parameters) beyond which the neglect of the final term of Eq. (24) is invalid. Wall rotation is shown to be ineffective at stabilizing the

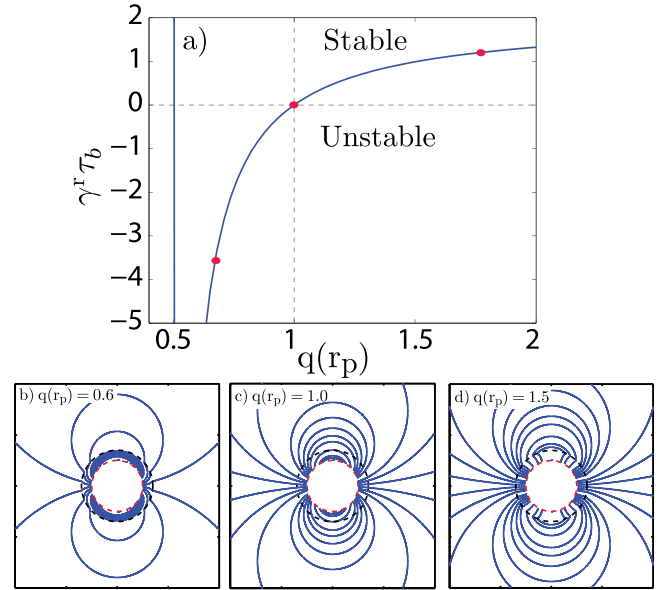


FIG. 12. (a) Time constants (eigenvalues) of the exponentially forced single wall system, with forcing specified in terms of the edge safety factor q . Field structures (eigenfunctions) at (b) $q(r_p) < 1$, (c) $q(r_p) = 1$, and (d) $q(r_p) > 1$.

mode in the single wall case as it does not modify γ^r in Eq. (31). Eigenfunctions at a few values of $q(r_p)$ are shown in Figs. 12(b)–12(d). Unstable ($q(r_p) < 1$) eigenfunctions are dipolar and inhibited from exiting the wall. The marginally stable ($q(r_p) = 1$) eigenfunction does not feel the wall at all, and stable ($q(r_p) > 1$) eigenfunctions have fieldlines which are inhibited from entering the wall. All cases are consistent with the condition $\gamma\tau_A \ll 1$.

2. Kink stabilization by wall rotation

The full two-wall dispersion relation of Eqs. (29) and (30) illustrates a scaling (shown in Fig. 13) very reminiscent of the vacuum field eigenmodes of Sec. IV C. Once again, the introduction of rotation tends to bring the two eigenmodes to a more common value, slowing the fast root and speeding up the slow root. However, now $\gamma = 0$ lies between the two roots when $q(r_p) < 1$. Raising the slow root thus requires it to transition through the stability threshold. Thus, stabilization of kink modes by wall rotation can be thought

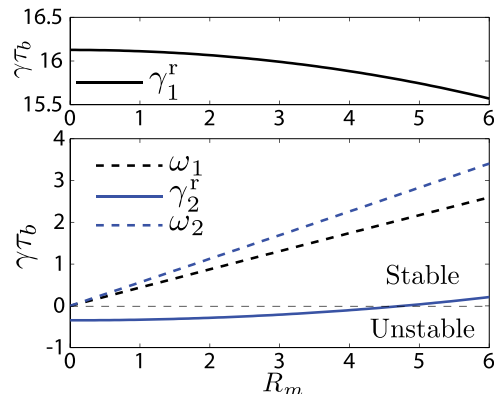


FIG. 13. Kink instability eigenvalues are brought towards a common value by wall rotation, as was the case with the vacuum eigenvalues shown in Fig. 10(a). At a critical R_m , the kink mode is stabilized.

of in terms of coupling the stable and unstable eigenmodes of the two-wall system. This theoretical result was first conceptualized by Gimblett,¹⁶ and was predicted for the lined system by Hegna.¹⁹ Subsequent experimental work has verified this prediction.^{30,34} Figure 13 illustrates that there is a critical R_m for stabilization of the kink mode, whose scaling was explored in Ref. 19 and is not repeated here.

C. Error field amplification

With the linear stability solved, attention is now turned to the driven stable modes predicted by Eq. (27). EFA (also called resonant field amplification) is calculated by finding the steady-state ($t \rightarrow \infty$) solution of Eq. (27) while allowing the forcing \vec{B}_{ext} to be finite. In the steady-state, $\frac{\partial}{\partial t} \rightarrow 0$ and \vec{A} is found by simple inversion of Eq. (27), such that $\vec{A}_{\text{EFA}} = (\bar{M}^{-1})\vec{B}_{\text{ext}}$, yielding

$$\vec{A}_{\text{EFA}} = \frac{2B_{\text{ext}}}{2 - iR_m \left(\frac{r_p^2}{r_b^2} \left(\frac{1}{1 - q(r_p)} \right) - 1 \right)} \left[\frac{1}{1 - q(r_p)} \right], \quad (32)$$

which gives the field structure in all regions after using the definitions for A_n given after Eq. (27). To evaluate the magnitude of the EFA, the predicted total field $\vec{B}_{\text{EFA}}|_{r=r_m}$ at a measurement location r_m (taken to be just outside r_p in region I) is normalized to the applied error field amplitude (B_{ext}). This yields

$$\frac{|B_{r,\text{EFA}}|}{B_{\text{ext}}} = \frac{\left| 1 - \frac{r_p^2}{r_m^2} \left(\frac{1}{1 - q(r_p)} \right) \right|}{\sqrt{1 + \frac{R_m^2}{4} \left(\frac{r_p^2}{r_b^2} \left(\frac{1}{1 - q(r_p)} \right) - 1 \right)^2}}. \quad (33)$$

As the fields are steady state, only the rotating wall interacts with the error field and thus Eq. (33) has no dependence on the inner wall parameters. Figure 14 illustrates the behavior of the EFA as R_m and $q(r_p)$ is varied. When $R_m = 0$, as $q(r_p) \rightarrow 1$ (the stability threshold) the EFA amplitude

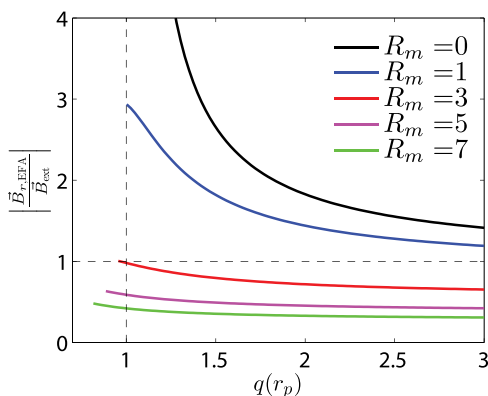


FIG. 14. The amount of EFA is shown as a function the safety factor ($q(r)$) and wall rotation R_m . At high $q(r_p)$ the error field is simply shielded, while at low $q(r_p)$ the wall rotation greatly reduces the amount of EFA.

diverges. However, unbounded growth breaks the steady-state assumption and thus the full treatment of Eq. (27) is required.²³ Nonetheless, the EFA can be expected to approach large values in this regime.

Finite R_m modifies this picture. First, shielding of B_{ext} occurs, such that in the high- $q(r_p)$ (stable plasma) limit Eq. (33) is identically equal to the vacuum field result of Eq. (7). Second, the linear stability threshold is brought to lower $q(r_p)$ as R_m increases, thus finite EFA is present at lower $q(r_p)$ whereas otherwise instability would result. Note the EFA is not calculated where the kink is unstable ($\gamma^r < 0$) as a steady state cannot be reached. Third, and most importantly, the actual amplitude of the EFA is decreased. This is thought to be because of a poorer overlap of the kink eigenmode to the applied error field at large R_m . As $R_m \rightarrow \infty$, the EFA vanishes.

VI. DISCUSSION

This work has shown that the superposition of error fields from external conductors and equilibrium plasma currents give rise to potentially significant asymmetries in wall rotation direction. These asymmetries were found to be the zeroth order effect of wall rotation on plasma dynamics in the rotating wall machine. In fact, the error field effect was initially misinterpreted as asymmetric stabilization of the kink mode in the device,³⁵ until experiments with a conducting rod revealed asymmetry without plasma. Later experiments elucidated the critical importance of this same error field to mode-locking bifurcations present in the device.^{29,30} Asymmetry in the error field naturally gives rise to asymmetries in mode-locking and other instability dynamics. Although toroidal effects are not treated here, future devices with flowing liquid metals may also exhibit similar error field asymmetries which then indirectly affect the plasma stability.

Section III D illustrated that the model developed to treat rigid conductors was also successful in capturing the asymmetries observed in stable plasma discharges. Vacuum superposition of \vec{B}_{ext} and \vec{B}_{eq} assumes that the two are independent of one another. This is not *a priori* guaranteed as the plasma can respond (move) due to \vec{B}_{ext} while the rigid rod cannot. That the vacuum superposition is valid for the stable plasma as well as the rigid conducting rod suggests that there is no appreciable modification of the error field by the stable plasma.

The result that the vertical field penetration time decreases as wall rotation increases is counterintuitive. Although infinite wall rotation yields a “perfectly conducting” wall, it does not simply increase the effective wall time. This work has shown that careful consideration of the multi-wall couplings is essential to build intuition on the effect of differential rotation on field eigenmodes. In the limit of an infinite number of walls, these results are reminiscent of the flowing liquid metal dynamo problem, where expected growth/decay constants are very sensitive functions of the flow profiles.³⁶ It is also clear that the success of the simple model to capture the experimental τ_{vfp} data indicates that the long-thin cylinder approximations made are very good.

EFA has been predicted to be mitigated by wall rotation in this study. Another model has also been developed to predict EFA (Refs. 22, 23, and 37) which predicts that the amplification factor scales as $\frac{\gamma_{\text{vac}}}{\gamma_{\text{kink}}}$ (Eqs. (16)–(18) in Ref. 22), where γ_{kink} would be the eigenvalue of the kink mode given by Eqs. (29) and (30) and γ_{vac} would be the vacuum field eigenvalue given by Eqs. (15) and (16). While the EFA as derived in Sec. V C varies somewhat with r_m , both methods yield broadly similar results for the impact of wall rotation on the EFA. In the model of Ref. 37, the reduction in amplification can be seen to be due to the imaginary parts of both γ_{vac} and γ_{kink} , present when $R_m \neq 0$. Inclusion of a finite imaginary component removes the divergence at marginal stability ($\gamma_{\text{kink}}^r \mapsto 0$). Additionally, the study of Ref. 23 is distinct from that treated herein due to the presence of differential wall rotation (multiple walls). Differential rotation precludes the use of Doppler shifts, and introduces non-linear Ω dependencies to both γ_{vac} and γ_{kink} .

ACKNOWLEDGMENTS

This work is supported by Department of Energy Grant Nos. DE-FG02-00ER54603 and DE-FG02-86ER53218, National Science Foundation Grant No. 0903900, and the National Science and Engineering Research Council Canada. The authors would like to thank M. Clark, J. Wallace, A. T. Echkart, E. S. Mueller, and J. Jara-Almonte for their assistance in performing experimental measurements. The authors also benefited from useful discussions with J. S. Sarff, J. M. Finn, I. V. Khalzov, and other individuals from the University of Wisconsin Plasma Physics Group and the Center for Magnetic Self-Organization.

¹A. H. Boozer, *Phys. Plasmas* **16**, 058102 (2009).

²J. D. Callen, *Nucl. Fusion* **51**, 094026 (2011).

³R. Fitzpatrick, *Nucl. Fusion* **33**, 1049 (1993).

⁴A. J. Cole, C. C. Hegna, and J. D. Callen, *Phys. Rev. Lett.* **99**, 1 (2007).

⁵K. C. Shaing, S. A. Sabbagh, and M. S. Chu, *Nucl. Fusion* **50**, 025022 (2010).

⁶A. M. Garofalo, W. M. Solomon, M. J. Lanctot, K. H. Burrell, J. C. DeBoo, J. S. DeGrassie, G. L. Jackson, J.-K. Park, H. Reimerdes, M. Schaffer, and E. J. Strait, *Phys. Plasmas* **16**, 056119 (2009).

⁷E. J. Strait, J. M. Bialek, N. Bogatu, M. S. Chance, M. S. Chu, D. H. Edgell, A. M. Garofalo, G. L. Jackson, R. J. Jayakumar, T. H. Jensen, O. N. Katsuro-Hopkins, J. S. Kim, R. J. La Haye, L. L. Lao, M. A. Makowski, G. A. Navratil, M. Okabayashi, H. Reimerdes, J. T. Scoville, A. D. Turnbull, and DIII-D Team, *Phys. Plasmas* **11**, 2505 (2004).

⁸J. Menard, M. G. Bell, R. E. Bell, and E. D. Fredrickson, *Nucl. Fusion* **43**, 330 (2003).

⁹S. A. Sabbagh, R. E. Bell, J. E. Menard, D. A. Gates, A. C. Sontag, J. M. Bialek, B. P. LeBlanc, F. M. Levinton, K. Tritz, and H. Yuh, *Phys. Rev. Lett.* **97**, 045004 (2006).

¹⁰A. H. Boozer, *Phys. Rev. Lett.* **86**, 5059 (2001).

¹¹M. J. Lanctot, H. Reimerdes, A. M. Garofalo, M. S. Chu, Y. Q. Liu, E. J. Strait, G. L. Jackson, R. J. La Haye, M. Okabayashi, T. H. Osborne, and M. Schaffer, *Phys. Plasmas* **17**, 030701 (2010).

¹²J.-K. Park, A. H. Boozer, J. E. Menard, and M. J. Schaffer, *Nucl. Fusion* **48**, 045006 (2008).

¹³R. J. Buttery, A. H. Boozer, Y. Q. Liu, J.-K. Park, N. M. Ferraro, V. Amoskov, Y. Gribov, R. J. La Haye, E. Lamzin, J. E. Menard, M. J. Schaffer, and E. J. Strait, *Phys. Plasmas* **19**, 056111 (2012).

¹⁴S. Bodner, V. Neil, and L. Smith, *Part. Accel.* **1**, 327 (1970).

¹⁵C. Ekdahl, *J. Appl. Phys.* **89**, 8214 (2001).

¹⁶C. G. Gimblett, *Plasma Phys. Controlled Fusion* **31**, 2183 (1989).

¹⁷C. G. Gimblett and R. J. Hastie, *Phys. Plasmas* **7**, 5007 (2000).

¹⁸M. V. Umansky, R. Betti, and J. P. Freidberg, *Phys. Plasmas* **8**, 4427 (2001).

¹⁹C. C. Hegna, *Phys. Plasmas* **11**, 4230 (2004).

²⁰S. I. Krasheninnikov, L. Zakharov, and G. V. Pereverzev, *Phys. Plasmas* **10**, 1678 (2003).

²¹L.-J. Zheng, M. T. Kotschenreuther, and F. L. Waelbroeck, *Nucl. Fusion* **46**, L9 (2006).

²²V. D. Pustovitov, *Nucl. Fusion* **47**, 1583 (2007).

²³V. D. Pustovitov, *Nucl. Fusion* **49**, 045003 (2009).

²⁴E. N. Parker, *Astrophys. J.* **122**, 293 (1963).

²⁵H. Moffatt, *Magnetic Field Generation in Electrically Conducting Fluids*, 1st ed. (Cambridge University, Cambridge, 1978).

²⁶M. Perry and T. Jones, *IEEE Trans. Magn.* **14**, 227 (1978).

²⁷M. Perry, *Low Frequency Electromagnetic Design*, 1st ed. (Taylor and Francis, Boca Raton, FL, 1985), p. 243.

²⁸C. Paz-Soldan, W. F. Bergerson, M. I. Brookhart, D. A. Hannum, R. D. Kendrick, G. Fiksel, and C. B. Forest, *Rev. Sci. Instrum.* **81**, 123503 (2010).

²⁹C. Paz-Soldan, M. I. Brookhart, A. T. Echkart, D. A. Hannum, C. C. Hegna, J. S. Sarff, and C. B. Forest, *Phys. Rev. Lett.* **107**, 245001 (2011).

³⁰C. Paz-Soldan, M. I. Brookhart, C. C. Hegna, and C. B. Forest, *Phys. Plasmas* **19**, 056104 (2012).

³¹Y. In, I. Bogatu, A. M. Garofalo, G. Jackson, J. Kim, R. La Haye, M. Lanctot, L. Marrelli, P. Martin, M. Okabayashi, H. Reimerdes, M. Schaffer, and E. J. Strait, *Nucl. Fusion* **50**, 042001 (2010).

³²M. Kruskal and M. Schwarzschild, *Proc. R. Soc. London, Ser. A* **223**, 348 (1954).

³³V. D. Shafranov, *At. Energ.* **5**, 38 (1956).

³⁴C. Paz-Soldan, M. I. Brookhart, A. J. Clinch, D. A. Hannum, and C. B. Forest, *Phys. Plasmas* **18**, 052114 (2011).

³⁵C. Paz-Soldan, W. F. Bergerson, M. I. Brookhart, D. A. Hannum, J. S. Sarff, C. C. Hegna, and C. B. Forest, in *Proceedings of IAEA Fusion Energy Conference (IAEA, Daejeon, S. Korea, 2010)*, pp. EXS/P5–05.

³⁶M. L. Dudley and R. W. James, *Proc. R. Soc. London, Ser. A* **425**, 407 (1989).

³⁷V. D. Pustovitov, *Plasma Phys. Rep.* **27**, 195 (2001).